Fluid Flows Control using Visual Servoing

R. Tatsambon Fomena, Christophe Collewet

Fluid Flows Control using Visual Servoing

Romeo Tatsambon Fomena and Christophe Collewet

Cemagref, INRIA Rennes-Bretagne Atlantique
and Université Européenne de Bretagne
(e-mails: romeo.tatsambon@inria.fr and christophe.collewet@inria.fr)

Abstract: This paper introduces for the first time the control of a fluid flow using visual servoing. The control consists to regulate a flow around a desired velocities profile. The originality here is the possibility to use optical flow measurements, computed from the observed flow, in a visual servo control scheme. Compared to existing approaches that uses a limited set of measurements to control a fluid flow, our approach is shown to be a major improvement in terms of the flow state estimation and control.

Keywords: Visual Servoing, Fluid flows control.

1. INTRODUCTION

The goal of this paper is to show the benefit of using vision-based control in a closed-loop scheme to control a fluid flow, that is to modify the current state of a flow in order to reach a desired state. Closed-loop vision-based control, also called visual servoing, is now a well established technique in the robotics community (see Espiau et al. (1992)). More precisely, to achieve a visual servoing task, a set of visual features $\mathbf{s}(t)$ is selected from the image of the scene. A control law is then designed so that this set of visual features $\mathbf{s}(t)$ reaches a desired value $\mathbf{s}^*$ corresponding to a desired state of the system. The dynamic of the error vector $\mathbf{e}(t) = \mathbf{s}(t) - \mathbf{s}^*$ is then given by

$$\dot{\mathbf{e}}(t) = \frac{\partial \mathbf{e}(t)}{\partial t} + \mathbf{L}_\mathbf{e}(t)\mathbf{u}(t), \tag{1}$$

where $\mathbf{u}$ is the system control inputs, $\mathbf{L}_\mathbf{e}(t)$ is the jacobian matrix encoding the time variation of the visual features to the variation of the control signal acting on the system and $\partial \mathbf{e}(t)/\partial t$ expresses the variation of the error vector due to the free motion of the visual features. The control principle is to regulate the error vector $\mathbf{e}$ to zero. The control law is built from (1) using the knowledge of the approximations $\widehat{\mathbf{L}_\mathbf{e}}(t)$ and $\widehat{\frac{\partial \mathbf{e}(t)}{\partial t}}$. Visual servoing has shown impressive results in numerous complex contexts such as underwater, medical and aerial (helicopters, blimp) robotic as shown in Bonin-Font et al. (2008).

In this work, we aim at stabilizing a flow, i.e. maintaining a flow in a desired state whatever the external perturbations. Fluid flows control is of great economical interest in aerospace. For instance reducing the drag of an airplane while enhancing lift can reduce fuel consumption. This can be done by preventing transition to a turbulent air flow around the plane wings.

Flows control can be achieved in two different ways: passive or active control. Passive control provides a permanent action on the system. Most often it consists in optimizing shapes or in choosing suitable surfacing (see Choi et al. (1993)). The main problem with this approach is that the control is, of course, inefficient when the system parameters change. Conversely, in active control an external energy is required to act on the system, such as techniques based on blowing and suction as described in Joshi et al. (1997). However, most often, only open-loop control is used. As a matter of fact, designing a closed-loop control law requires the use of sensors that can be at the same time non-intrusive, accurate and adapted to the time and space scale of the phenomenon under monitoring. Unfortunately, such sensors are hardly available in the real context of control applications. The most commonly used measurement, obtained from MEMS, is the shear stress at a limited set of measurement points (see Joshi et al. (1997)).

To deal with these issues, we propose a closed-loop vision-based control approach. As far as we know, the proposed approach has never been used for flows control issues. By using vision, the complete flow can be fully observed in real time (see Champagnat et al. (2009)). This full observation is shown to be of great improvements for flows control in comparison with existing control approaches that use only a limited set of walls shear stress measurements.

In this paper, we focus on 2D plane Poiseuille flow which is well-known in fluid mechanics. The control framework for this flow is presented in Section 2. We then compare, in Section 3, the existing control approaches and the proposed vision-based control approach. In Section 4, the proposed theoretical results are validated in simulation using synthetic data sets of spatio-temporal variations of flow velocities.

2. 2D PLANE POISEUILLE FLOW MODELING FOR CONTROL DESIGN

In this section we first present the basics of Poiseuille flow, then we introduce the control principle for this flow and finally we present the reduced linearized model used to derive the existing shear stress based control laws.

2.1 Basics of the Poiseuille flow

Poiseuille flow is a flow in an infinite length channel due to a pressure gradient. Fig. 1 illustrates the steady

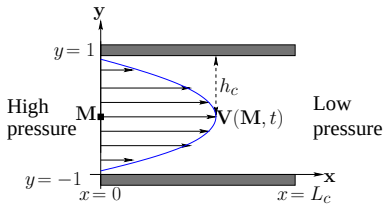

Fig. 1. Steady state velocities profile of the 2D plane Poiseuille flow: h_c is the channel half height, L_c is the flow streamwise period length and $\mathbf{M}$ is a point in the flow.

state velocities profile of the plane Poiseuille flow in a streamwise period of the infinite length channel. The non dimensionalized Navier-Stokes equation of this flow is given by

$$\begin{cases} \dfrac{\partial \mathbf{V}}{\partial t} + (\boldsymbol{\nabla}\mathbf{V})\mathbf{V} = -\boldsymbol{\nabla}P + \dfrac{1}{R_e}\boldsymbol{\nabla}^2\mathbf{V} \\ \boldsymbol{\nabla}\cdot\mathbf{V} = 0 \\ \mathbf{V}(x, y=\pm 1, t) = \mathbf{0} \end{cases} \tag{2}$$

where P is the pressure; $\mathbf{V}$ is the flow velocity; $\mathbf{V}(x, y=\pm 1, t) = \mathbf{0}$ represents the no slip boundary condition ; R_e is a dimensionless number called the Reynolds number.

Since the Poiseuille flow is simple, the analytical solution (V_{bx}, V_{by}, P_b) of (2) in the steady state case, i.e. $\frac{d\mathbf{V}}{dt} = \frac{\partial \mathbf{V}}{\partial t} + \mathbf{V}\cdot\boldsymbol{\nabla}\mathbf{V} = \mathbf{0}$, can be found:

$$(V_{bx}, V_{by}, P_b) = (1-y^2, 0, -\frac{2}{R_e}x). \tag{3}$$

This solution is illustrated in Fig. 1.

2.2 Control principle of the Poiseuille flow

A 2D Plane flow Poiseuille flow can be controlled via boundaries. Boundary control consists in modifying the upper and lower boundary conditions (see Joshi et al. (1997)). The boundary control on the upper and the lower channels can be theoretically represented by functions χ_u and χ_l that allows mass conservation in the controlled system as pictured in Fig. 2. Note that in the absence of control the red dashed curves (see Fig. 2) are aligned with the lower and upper boundary lines as expected.

The existing active control approaches, presented in Joshi et al. (1997), Bewley and Liu (1998) and McKernan (2006), focus on the stabilization of the flow, i.e. maintaining the flow in a desired state, typically the steady state, whatever the external perturbations. In this case the flow is initially in the steady state but in an unstable equilibrium, i.e. a small velocities pertubation value $\mathbf{V_p}(x, y, t)$ destabilizes the non-controlled fluid flow.

2.3 Reduced linearized model of Poiseuille flow

The modeling, required to derive the control law, consists first of all in linearizing the Navier-Stokes equation (NSE) around the steady state solution. Then the continuous linearized model of the NSE of the flow is first represented in the Fourier domain at a specific wavenumber $\alpha_n = 2\pi/L_c$ containing the instability: $\mathbf{V_p}(x, y, t) = \mathbf{V_p^n}(y, t)e^{j\alpha_n}$. Then the obtained spectral representation $\mathbf{V_p^n}(y, t)$ is discretised in the y direction by

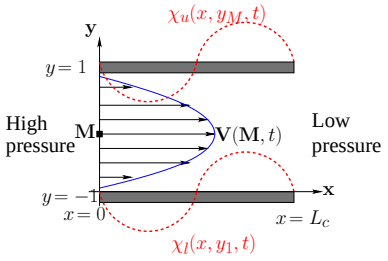

Fig. 2. Boundaries control.

using a number of M Gauss-Lobatto collocation points $y_k = \cos\left((k-1)\pi/(M-1)\right),\ 1 \le k \le M$. Gauss-Lobatto collocation points are chosen to improve the spectral accuracy. The obtained reduced linearized model is given by (see McKernan (2006)):

$$\begin{cases} \dot{\mathbf{p}}^{\mathbf{n}}(t) = \mathbf{A^n}\mathbf{p^n}(t) + \mathbf{B^n}\mathbf{u}(t) \\ \mathbf{z}(t) = \mathbf{C}^{\top\mathbf{n}}\mathbf{p^n}(t) \\ \mathbf{p^n}(0) = \mathbf{p^n}_0 \end{cases} \tag{4}$$

where $\mathbf{p^n}(t)$ is the state vector, $\mathbf{A^n}$ is the state matrix, $\mathbf{u}(t)$ is the system input, like blowing or suction actions on the channel boundaries, $\mathbf{B^n}$ is the input matrix, $\mathbf{C^n}$ is the output matrix and $\mathbf{z}(t)$ is the vector of shear stress measurements on the upper and lower boundaries.

In the classical case (see Joshi et al. (1997), McKernan (2006), Bewley and Liu (1998)) of Reynolds number $Re = 10\,000$ and wavenumber $\alpha_n = 1$, the reduced linearized model of Poiseuille flow (4) is unstable as shown in Orszag (1971). This instability can be seen through the poles of the state matrix $\mathbf{A^n}$. These poles are illustrated on Fig. 3, where we can see the unstable mode $\lambda = 0.00373967 \pm i0.23752649$. Control theory for linear systems can be used to cancel this instability.

In the next section, we compare the existing control approaches with our vision-based approach.

3. COMPARISON OF THE CONTROL APPROACHES

3.1 Existing control approaches

Using the classical output feedback control $\mathbf{u}(t) = -\mathbf{k}^\top\mathbf{z}(t)$, the controller generally fails to suppress unobservable high transient modes which could trigger transition to turbulence as shown in Joshi et al. (1997). The currently existing approaches focus on the state feedback LQR (see McKernan (2006)) and the output feedback LQG regulation (see Bewley and Liu (1998)). While the LQR approach can not be used in practice since it requires the knowledge of the true state value $\mathbf{p^n}(t)$, the LQG approach is built on an observer. This observer provides an estimated value $\widehat{\mathbf{p^n}}(t)$ of the state vector from the shear stress measurements $\mathbf{z}(t)$ using a Linear Quadratic Estimation (LQE) scheme. The control signal for the output feedback LQG regulator is thus given by

$$\mathbf{u}(t) = -\mathbf{k}^\top\widehat{\mathbf{p^n}}(t), \tag{5}$$

where vector $\mathbf{k}$ is the LQR optimal gain.

In the next section we focus on state estimation using an observer in existing approaches and using optical flow measurements in our approach.

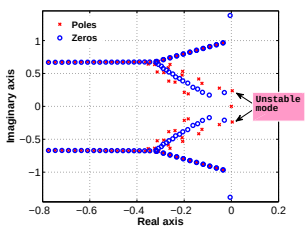

Fig. 3. Poles and zeros of the reduced linearized system.

3.2 Flow State estimation

Before presenting the vision-based state estimation approach we briefly recall the LQE of the state vector using a limited number of shear stress measurements.

3.2.1. Existing LQE state estimation. In the LQE framework it is supposed that the reduced linearized system (4) has process disturbances $\boldsymbol{\varepsilon}_{\mathbf{p}}$ and measurements noise $\boldsymbol{\varepsilon}_z$. In addition $\boldsymbol{\varepsilon}_{\mathbf{p}}$ and $\boldsymbol{\varepsilon}_z$ are uncorrelated Gaussian white noise with covariance matrices $\Xi_{\mathbf{p}}$ and Ξ_z respectively. The reduced linearized system (4) is thus rewritten as

$$\begin{cases} \dot{\mathbf{p}}^{\mathbf{n}}(t) = \mathbf{A}^{\mathbf{n}}\mathbf{p}^{\mathbf{n}}(t) + \mathbf{B}^{\mathbf{n}}\mathbf{u}(t) + \boldsymbol{\varepsilon}_{\mathbf{p}}(t) \\ \mathbf{z}(t) = \mathbf{C}^{\top\mathbf{n}}\mathbf{p}^{\mathbf{n}}(t) + \boldsymbol{\varepsilon}_z(t) \\ \mathbb{E}\left\{\boldsymbol{\varepsilon}_{\mathbf{p}}\boldsymbol{\varepsilon}'_{\mathbf{p}}\right\} = \Xi_{\mathbf{p}},\ \mathbb{E}\left\{\boldsymbol{\varepsilon}_z\boldsymbol{\varepsilon}'_z\right\} = \Xi_z \\ \mathbb{E}\left\{\boldsymbol{\varepsilon}_z\boldsymbol{\varepsilon}'_{\mathbf{p}}\right\} = \mathbf{0},\ \mathbb{E}\left\{\boldsymbol{\varepsilon}_{\mathbf{p}}\boldsymbol{\varepsilon}'_z\right\} = \mathbf{0} \\ \mathbf{p}^{\mathbf{n}}(0) = \mathbf{p}^{\mathbf{n}}{}_0, \end{cases} \tag{6}$$

where $\mathbf{x}'$ denotes the conjugate transpose of vector $\mathbf{x}$.

From the plant model given in (6), the state vector LQE is given by

$$\begin{cases} \dot{\widehat{\mathbf{p}^{\mathbf{n}}}}(t) = \mathbf{A}^{\mathbf{n}}\widehat{\mathbf{p}^{\mathbf{n}}}(t) + \mathbf{B}^{\mathbf{n}}\mathbf{u}(t) + \mathbf{L}(\mathbf{z}(t) - \mathbf{C}^{\mathbf{n}\top}\widehat{\mathbf{p}^{\mathbf{n}}}(t)) \\ \widehat{\mathbf{p}^{\mathbf{n}}}(0) = \mathbf{unknown}, \end{cases} \tag{7}$$

where $\widehat{\mathbf{p}^{\mathbf{n}}}(t)$ is the estimated state vector, and $\mathbf{L}$ the LQE optimal gain. From (6) and (7), the estimation error dynamic is given by

$$\begin{cases} \dot{\widehat{\mathbf{p}^{\mathbf{n}}}}(t) - \dot{\mathbf{p}}^{\mathbf{n}}(t) = (\mathbf{A}^{\mathbf{n}} - \mathbf{L}\mathbf{C}^{\mathbf{n}\top})(\widehat{\mathbf{p}^{\mathbf{n}}}(t) - \mathbf{p}^{\mathbf{n}}(t)) + \mathbf{L}\boldsymbol{\varepsilon}_z(t) - \boldsymbol{\varepsilon}_{\mathbf{p}}(t) \\ \widehat{\mathbf{p}^{\mathbf{n}}}(0) - \mathbf{p}^{\mathbf{n}}(0) = \mathbf{unknown}. \end{cases} \tag{8}$$

A well-known key issues in the LQE is the choice of the initial value $\widehat{\mathbf{p}^{\mathbf{n}}}(t=0)$ that has to be fed to the observer (see 7)). Indeed this initial value highly influences the convergence time after which $\widehat{\mathbf{p}^{\mathbf{n}}}(t)$ equals the true value of the state vector $\mathbf{p}^{\mathbf{n}}(t)$. Modeling the initial condition $\widehat{\mathbf{p}^{\mathbf{n}}}(t=0)$ with known physical statistics about the studied flow and using a time-varying estimator gain $\mathbf{L}(t)$ can reduce the time to which $\widehat{\mathbf{p}^{\mathbf{n}}}(t)$ equals the true value of the state vector $\mathbf{p}^{\mathbf{n}}(t)$ as proposed in Hœpffner et al. (2005). But this solution is still not satisfactory since it needs additional a-priori parameters in the model of the initial condition. In addition, it is also well-known that the above presented LQE approach produces a noisy estimation when shear measurements are noisy (see (8)). The initialization and the noise issues in the LQE could provoke turbulence in the controlled flow and divergence of the control as shown in McKernan (2006).

3.2.2. Vision-based state estimation in the general case of noisy measurements. In this section, we overcome the above mentioned issues related to state vector estimation

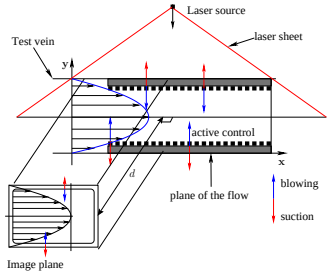

Fig. 4. Visualization of the flow using a laser sheet which role is to enlighten the particles seeded in the fluid.

by using optical flow measurements as shown in Fig. 4. Optical flow is the apparent velocity vector field representing the motion of photometric pattern (pixels luminance) in successive image sequences. Optical flow techniques can be used to estimate instantaneous velocities of a fluid flow from any image sequences as detailed in Heitz et al. (2010).

Our contribution relies on the fact that from the knowledge of the optical flow it is possible to estimate the flow perturbation velocities field $\mathbf{V}_{\mathbf{p}}(x,y,t)$ and therefore to compute the estimation $\widehat{\mathbf{p}^{\mathbf{n}}}(t)$ of the state vector. The initial value $\widehat{\mathbf{p}^{\mathbf{n}}}(t=0)$ is therefore no longer of concerned in our approach. This estimation is used thereafter in a closed-loop LQR scheme: the obtained closed-loop LQR is thus a visual servoing control scheme. Indeed using $\mathbf{s}(t) = \mathbf{p}^{\mathbf{n}}(t)$, around the steady state, the error dynamic given by (1) is identified as the first equation in (4).

The optical flow can be obtained from the fronto-parallel projection on the 2D flow (see Fig. 4) using the technique described in Heitz et al. (2010). The obtained image velocties field is exactly $\frac{1}{d}\mathbf{V}_{\mathbf{p}}(x,y,t)$ which is proportional to the 2D flow perturbation velocity $\mathbf{V}_{\mathbf{p}}(x,y,t)$ up to the scale factor $d > 0$ (distance between the flow plane and the image plane). In the following we assume that the distance d is obtained by a calibration technique, in which case we can measure the flow velocity field $\mathbf{V}_{\mathbf{p}}(x,y,t)$.

Let $\boldsymbol{\varepsilon}(x,y,t)$ be a 2D independent identically distributed white Gaussian process. Let $\mathbf{V}_{\mathbf{p}}$ be the $M \times N$ pixels size image of the pertubation velocity obtained from noise-free optical flow measurements. In the practical case where optical flow measurements provide noisy velocity perturbation $\widehat{\mathbf{V}_{\mathbf{p}}}(x,y,t) = \mathbf{V}_{\mathbf{p}}(x,y,t) + \boldsymbol{\varepsilon}(x,y,t)$, these noisy measurements are used to compute estimation of the state vector $\widehat{\mathbf{p}^{\mathbf{n}}}(t)$ as shown in Appendix A. The estimated state vector is given by

$$\widehat{\mathbf{p}^{\mathbf{n}}}(t) = \mathbf{p}^{\mathbf{n}}(t) + \frac{1}{N}\mathbf{e}^{\mathbf{n}}(t), \tag{9}$$

where vector $\mathbf{e}^{\mathbf{n}}(t)$ is related to the measurements noise matrix $\boldsymbol{\varepsilon}(x,y,t)$. It is clear from (9), that the larger the value of N the closer $\widehat{\mathbf{p}^{\mathbf{n}}}(t)$ is from $\mathbf{p}^{\mathbf{n}}(t)$.

Now we compare the behavior of the system closed with the two control approaches.

3.3 Comparison of the behavior of the closed-loop systems

3.3.1. Behavior of the system closed by the LQG control. Combining the estimation error dynamic given in (8) and the LQR state dynamic (plugging (5) into the first equation of (6)), we obtain

$$\begin{cases} \begin{bmatrix} \dot{\mathbf{p}}^{\mathbf{n}}(t) \\ \dot{\widehat{\mathbf{p}^{\mathbf{n}}}}(t) - \dot{\mathbf{p}}^{\mathbf{n}}(t) \end{bmatrix} = \mathbf{M}_{lqg} \begin{bmatrix} \mathbf{p}^{\mathbf{n}}(t) \\ \widehat{\mathbf{p}^{\mathbf{n}}}(t) - \mathbf{p}^{\mathbf{n}}(t) \end{bmatrix} + \mathbf{M}_n \begin{bmatrix} \boldsymbol{\varepsilon}_{\mathbf{p}}(t) \\ \varepsilon_z(t) \end{bmatrix} \\ \widehat{\mathbf{p}^{\mathbf{n}}}(0) - \mathbf{p}^{\mathbf{n}}(0) = \mathbf{unknown} \end{cases} \tag{10}$$

where $\mathbf{M}_{lqg} = \begin{bmatrix} \mathbf{A^n} - \mathbf{B^n k}^\top & -\mathbf{B^n k}^\top \\ \mathbf{0} & \mathbf{A^n} - \mathbf{L C}^{\top \mathbf{n}} \end{bmatrix}$ and $\mathbf{M}_n = \begin{bmatrix} \mathbf{I} & \mathbf{0} \\ -\mathbf{I} & \mathbf{L} \end{bmatrix}$, with $\mathbf{I}$ an identity matrix. Equation (10) shows that the true state dynamic $\dot{\mathbf{p}}^{\mathbf{n}}(t)$ depends on $\widehat{\mathbf{p}^{\mathbf{n}}}(t)$ and on $\mathbf{p}^{\mathbf{n}}(0)$. Therefore, a poor initialization of the observer could cause the divergence of the non-linear system describing the fluid flow. In addition the noise in the measurements propagates (see (10)) in the control law (see (5)); and this is not suitable for actuators in practice.

3.3.2. Behavior of the system closed by the vision-based control. In the case of measurements noise in the optical flow, the reduced linearized system (4) controlled by the vision-based approach is given by

$$\begin{cases} \dot{\mathbf{p}}^{\mathbf{n}}(t) = \mathbf{A^n p^n}(t) + \mathbf{B^n u}(t) \\ \mathbf{u}(t) = -\mathbf{k}^\top \widehat{\mathbf{p}^{\mathbf{n}}}(t) \\ \widehat{\mathbf{p}^{\mathbf{n}}}(t) = \mathbf{p}^{\mathbf{n}}(t) + \dfrac{1}{N}\mathbf{e}^{\mathbf{n}}(t), \end{cases} \tag{11}$$

where $\mathbf{k}$ is the LQR optimal gain. The closed-loop reduced linearized system (11) can be rewritten as

$$\dot{\mathbf{p}}^{\mathbf{n}}(t) = (\mathbf{A^n} - \mathbf{B^n k}^\top)\mathbf{p}^{\mathbf{n}}(t) - \frac{1}{N}\mathbf{B^n k}^\top \mathbf{e}^{\mathbf{n}}(t). \tag{12}$$

The initial value $\widehat{\mathbf{p}^{\mathbf{n}}}(t=0)$ is therefore no longer of concerned in our approach. In addition for a large number of pixels N, the reduced linearized system dynamic equation (12) is less affected by measurements noise since $\frac{1}{N}\mathbf{B^n k}^\top \mathbf{e}^{\mathbf{n}}(t)$ tends to $\mathbf{0}$. This is another great improvement over the LQG control scheme that is always noise dependent when noisy shear stress values are used in the LQE as shown in (10).

4. RESULTS

In this section the validations of our approach do not use real optical flow measurements. We use synthetic data sets of spatio-temporal variations of the perturbation velocities $\mathbf{V_p}(x, y, t)$ obtained from the Poiseuille flow reduced linearized model presented in (4). This reduced linearized model is used to build a linear simulator of 2D channel Poiseuille flow with the following classical characteristics as used in related works Joshi et al. (1997), Bewley and Liu (1998) and McKernan (2006): the Reynolds number is $R_e = 10\ 000$, the length of the channel is $L_c = 4\pi$, and the reduced model Fourier wavenumber that contains instabilities is $\alpha_n = 1$. Using Matlab codes provided in McKernan (2006), matrices $\mathbf{A^n}$, $\mathbf{B^n}$, $\mathbf{C^n}$ given in (4) are computed. The optimal gain $\mathbf{k}$ is computed from the weighting matrix $\mathbf{R}$ set as a scaled identity matrix $\mathbf{R} = r\mathbf{I}$ with $r = 200$, penalizing thus high control values; and from the weighting matrix $\mathbf{Q}$ developed to compute the kinetic energy density $\mathcal{E}(t) = \mathbf{p^{n\prime}}(t)\mathbf{Q}\mathbf{p^n}(t)$ in McKernan (2006) .

We first present results concerning the vision-based control approach in the ideal case where there is no measurements noise. Fig. 5 shows the different steps in the control of the perturbed flow with $N_x = 252$. Fig. 5(a) pictures the desired image of the flow corresponding to the steady state velocities profile; Fig. 5(b) shows the image of the flow

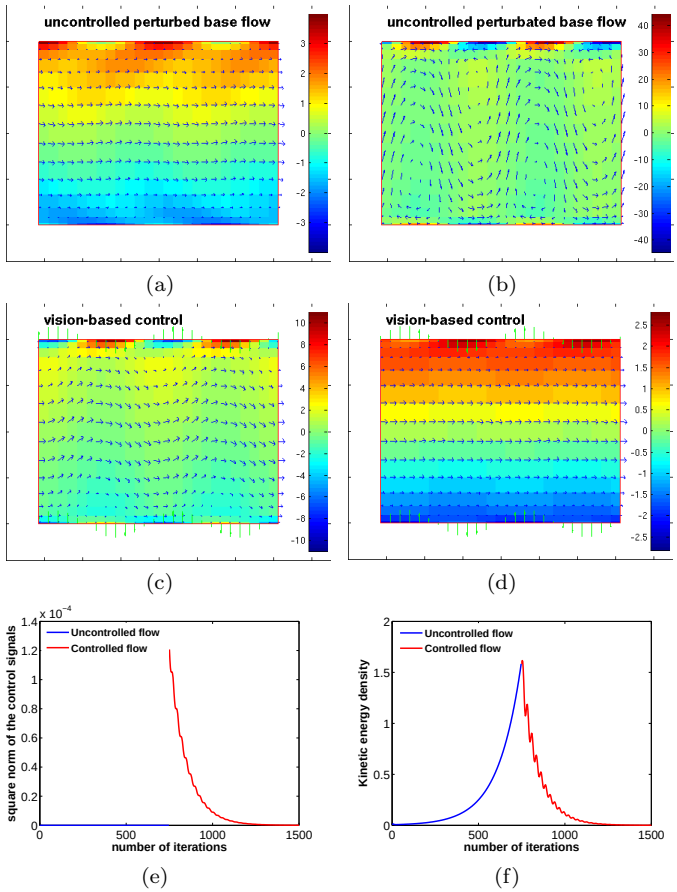

Fig. 5. Vision-based control (the color in the figures represents the vorticity map): (a) desired image of the flow, (b) initial image of the flow, the perturbation has grown $k = 750$, (c) controlled flow at $k = 1047$, (d) controlled flow at $k = 1500$, (e) control law versus frame iteration and (f) kinetic energy density versus frame iteration.

just before the application of the vision-based control law where we can see that the flow has become turbulent. Figs. 5(c) and 5(d) show different steps of the controlled flow at arbitrary selected iteration numbers $k = 1047$ and $k = 1500$ respectively: the control at each selected instant is represented by green vertical arrows on the upper and the lower channel boundaries. The control law converges since it tends towards 0 as shown on Fig. 5(e). Moreover, Fig. 5(f) depicts the kinetic energy density of the flow perturbation where we can see an increase due to the pertubation growth in the case where the flow is not controlled; and then a decrease also towards 0 once the control law is applied. At this step, we can see that the final velocities profile given in Fig. 5(d) is very similar to the desired velocities profile in Fig. 5(a). Therefore, the vision-based approach performs as expected.

4.1 Comparison of the estimation methods

In this section we show that the vision-based state estimation provides better results than the LQE. We consider a perturbed flow that is not controlled. Results are given in Fig. 6 in terms of the square norm of the state vector instead of the more relevant $2M$ (normally greater than 40 for a more accurate reduced model (4)) components

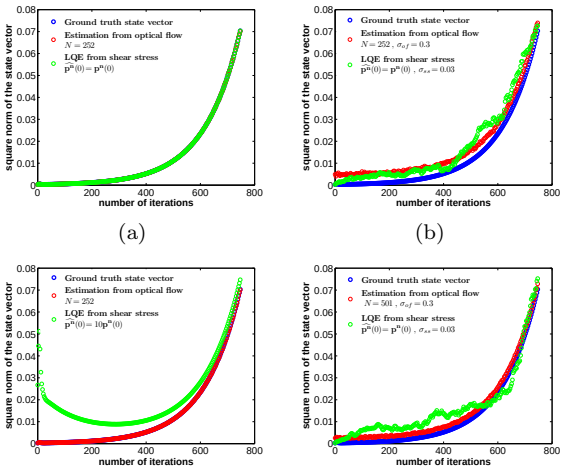

Fig. 6. Comparison of state vector estimations using shear stress and optical flow: (a) ideal case, (b) measurements noise, (c) LQE initialization, (d) measurements noise with a large number of pixels N.

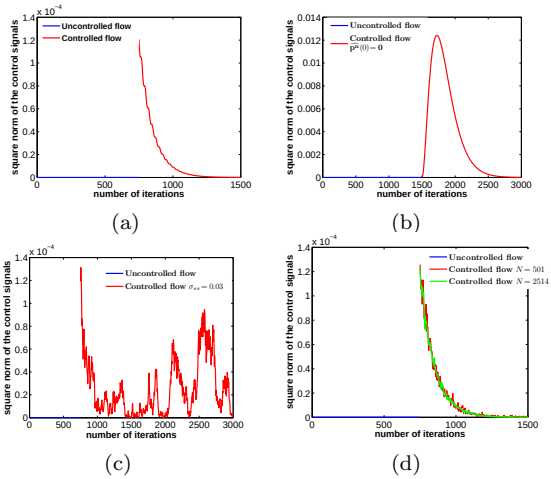

Fig. 7. Comparison LQG and the vision-based control approaches: (a) ideal case, (b) initialization error in the LQG regulator, (c) measurements noise in the LQG regulator, (d) measurements noise in the vision-based control.

of the state vector for the sake of clarity and readability. Fig. 6(a) presents the ideal case where there is no measurements noise and no initialization error. From this figure we can see that both estimations perfectly correspond to the ground truth value of the state vector. Fig. 6(c) highlights the initialization and the asymptotic convergence issues in the LQE; these issues are not of concerned in the vision-based approach which provides the ground truth value of the state vector. This result confirmes that the optical flow based estimation performs better than the LQE from shear stress measurements in any case.

The strong robustness to noise of the vision-based state estimation is presented on the right column figures where the standard deviation (STD) σ_{of} on the optical flow noise is purposely set to a value 10 times higher than the STD σ_{ss} on the shear stress noise. These figures present an average over a large number of realizations of the stochastic noises. Using only $N = 252$ pixels on the streamwise direction, Fig 6(b) shows a poor vision-based state estimation compared to Fig. 6(d) where $N = 501$ pixels are used. Note that $N = 501$ is far less than the number of pixels available in real situations where the images size can be at least 1280×960 ($N = 1280$). Due to a large number of flow velocities provided by the optical flow, the new approach is very robust to noisy measurements.

4.2 Behavior of the closed-loop systems

The behavior of the closed-loop system is shown to be better with the visio-based control than with the LQG control. Results are presented in Fig. 7. Fig. 7(a) depicts the behavior of the control signal in the ideal case (no measurements noise, no initialization error). Fig. 7(b) depicts the behavior of the control signal when the initial value is set as $\widehat{\mathbf{p^n}}(0) = \mathbf{0}$ by default since the value of $\widehat{\mathbf{p^n}}(0)$ is unknown. In this case we can see that the value of the control signal is 100 times higher than the ideal control signal case which includes the vision-based approach (compare the highest control signal values in Fig. 7(b) and 7(a)). This higher control signal value could lead to an unsuitable state trajectory which can cause the real non-linear system to diverge as shown in McKernan (2006). In addition, as expected, the control signal (see Fig. 7(b)) takes more time to converge to 0 (3000 iterations compared to the VB-LQG approach). This leads to an energy consumption far much higher for the LQG control than for the vision-based control.

The figures in the second row present the control signals in presence of measurements noise. Fig. 7(c) pictures the case of LQG control where we can see that the control signal does not converge to zero. Although the noise STD has been set to a small value, $\sigma_{ss} = 0.03$, the control signal is very noisy, which is not suitable for actuators. Finally, Fig. 7(d) illustrates the robustness of the vision-based control where the STD in the optical flow noise is 10 times higher than the STD in the shear stress noise: we can see from this last figure that the control converges, and we can also see that the larger the sample of flow particles velocities used the lesser the noise in the control signal.

5. CONCLUSION

In this paper we have proposed a new approach for fluid flows control. This approach is based on optical flow techniques, which are non-intrusive, robust to measurements noise and thus suitable for fluid flows control. Theoretical proofs has been presented in order to show the improvements provided by the vision-based approach over the commonly used output feedback LQG control in terms of the state vector estimation and flows control. Indeed the output feedback LQG limitations concern the initialization of the observer and measurements noise. The initialization issue is not of concerned in the vision-based approach which provides lower control signal values than the LQG scheme in the case of an initialization error. In addition the vision-based approach has been shown to be robust to measurements noise since a large number of flow velocities is available in real practical situations. Future works will focus on a real implementation of the proposed approach.

REFERENCES

Bewley, T. and Liu, S. (1998). Optimal and robust control and estimation of linear paths to transition. *J. Fluid Mech.*, 365, 305–349.

Bonin-Font, F., Ortiz, A., and Oliver, G. (2008). Visual navigation for mobile robots: a survey. *Journal of Intelligent & Robotic Systems*, 53(3), 263–296.

Champagnat, F., Plyer, A., Le Besnerais, G., Leclaire, B., and Le Sant, Y. (2009). How to calculate dense piv vector fields at video rate. In *8th Int. Symp. On Particle Image Velocimetry*. Melbourne, Victoria (Australia).

Choi, H., Moin, P., and Kim, J. (1993). Direct numerical simulation of turbulent flow over riblets. *J. Fluid Mech.*, 255, 503–539.

Espiau, B., Chaumette, F., and Rives, P. (1992). A new approach to visual servoing in robotics. *IEEE Trans. on Robotics and Automation*, 8(3), 313–326.

Heitz, D., Mémin, E., and Schnörr, C. (2010). Variational fluid flow measurements from image sequences: synopsis and perspectives. *Exp. Fluids*, 48(3), 369–393.

Hœpffner, J., Chevalier, M., Bewley, T., and Henningson, D. (2005). State estimation in wall-bounded flow systems. part 1. perturbed laminar flows. *J. Fluid Mech.*, 534, 263–294.

Joshi, S., Speyer, J., and Kim, J. (1997). A systems theory approach to the feedback stabilization on infinitesimal and finite amplitude disturbances in plane Poiseuille flow. *J. Fluid Mech.*, 332, 157–184.

McKernan, J. (2006). *Control of plane Poiseuille flow: a theoretical and computational investigation*. Ph.D. thesis, Cranfield University.

Orszag, S. (1971). Accurate solution of the Orr-Sommerfeld stability equation. *J. Fluid Mech.*, 50, 689–703.

Appendix A. VISION-BASED STATE ESTIMATION

In this worth mentioning that only the normal component $\mathbf{V_{py}}(x,y,t)$ of the perturbation velotiy $\mathbf{V_p}(x,y,t)$ is used to compute the state vector $\mathbf{p^n}(t)$ given in (4) (see McKernan (2006)). Here we show the three steps for estimation of $\widehat{\mathbf{p^n}}(t)$ (given by (9)) from the optical flow field measurements $\widehat{\mathbf{V_{py}}}(y,x,t)$ (transpose of $\widehat{\mathbf{V_{py}}}(x,y,t)$) in the general case where measurements are corrupted by noise:

$$\widehat{V_{py}}(y_k,x_i,t) = V_{py}(y_k,x_i,t) + \varepsilon_{ki}(t) \qquad \text{(A.1)}$$

where $\varepsilon_{ki}(t)$ is an idd Gaussian noise on the velocity value at each pixel with standard deviation (STD) σ_{of} and 0 mean; $k=1,...,M$; $i=1,...,N$.

We first compute the Fourier series coefficients of the measured image velocities $\widehat{\mathbf{V_{py}}}$ at the wavenumber $\alpha_n = 1$. Indeed by multiplying $\widehat{\mathbf{V_{py}}} = \left(\widehat{V_{py}}(y_k,x_i,t)\right)_{k=1,...,M,\ i=1,...,N}$ by the transpose of the vector $\frac{1}{N}\left[\, e^{-j\alpha_n x_1} \ \cdots \ e^{-j\alpha_n x_M} \,\right]$, we obtain the Fourier series of the noisy velocities $\widehat{V_{py}^n} = \left(\widehat{V_{py}^n}(y_k,t)\right)_k$ with

$$\widehat{V_{py}^n}(y_k,t) = V_{py}^n(y_k,t) + \frac{1}{N}\varepsilon_k^n(t), k=1,...,M \qquad \text{(A.2)}$$

Since the upper boundary condition is a sinusoidal function, its Fourier series coefficient is given by

$$\widehat{V_{py}^n}(y_1,t) = \widehat{q_u^n}(t) f_u(y_1), \qquad \text{(A.3)}$$

from which we deduce that

$$\widehat{q_u^n}(t) = \frac{1}{f_u(y_1)} V_{py}^n(y_1,t) + \frac{1}{N f_u(y_1)}\varepsilon_1^n(t). \qquad \text{(A.4)}$$

Plugging $q_u^n(t) = \frac{1}{f_u(y_1)} V_{py}^n(y_1,t)$ into (A.4) leads to

$$\widehat{q_u^n}(t) = q_u^n(t) + \frac{1}{N f_u(y_1)}\varepsilon_1^n(t). \qquad \text{(A.5)}$$

Similarly the coefficient $\widehat{q_l^n}(t)$ for the lower boundary can be expressed as

$$\widehat{q_l^n}(t) = q_l^n(t) + \frac{1}{N f_l(y_M)}\varepsilon_M^n(t). \qquad \text{(A.6)}$$

In the second step we compute the homogeneous coefficients vector $\widehat{\mathbf{V_{py}^{hn}}}$. These homogeneous coefficient measurements $\widehat{V_{py}^{hn}}(y_k,t)$ are given by the expression

$$\widehat{V_{py}^h}(y_k,t) = \widehat{V_{py}}(y_k,t) - \widehat{q_u^n}(t) f_u(y) - \widehat{q_l^n}(t) f_l(y). \qquad \text{(A.7)}$$

Using (A.2), (A.5) and (A.6), it is easy to rewritte expression (A.7) as

$$\widehat{V_{py}^{hn}}(y_k,t) = V_{py}^{hn}(y_k,t) + \frac{1}{N}\varepsilon_k^{hn}(t), \qquad \text{(A.8)}$$

where $\varepsilon_k^{hn}(t) = \left(\varepsilon_k^n(t) - \frac{f_u(y_k)}{f_u(y_1)}\varepsilon_1^n(t) - \frac{f_l(y_k)}{f_l(y_M)}\varepsilon_M^n(t)\right)$. The homogeneous coefficients vector is thus given by

$$\begin{bmatrix} 0 \\ \widehat{V_{py}^{hn}}(y_2,t) \\ \vdots \\ \widehat{V_{py}^{hn}}(y_{M-1},t) \\ 0 \end{bmatrix} = \begin{bmatrix} 0 \\ V_{py}^{hn}(y_2,t) \\ \vdots \\ V_{py}^{hn}(y_{M-1},t) \\ 0 \end{bmatrix} + \frac{1}{N}\begin{bmatrix} 0 \\ \varepsilon_2^{hn}(t) \\ \vdots \\ \varepsilon_{M-1}^{hn}(t) \\ 0 \end{bmatrix}. \qquad \text{(A.9)}$$

In the last step, the result of projection of $\widehat{V_{py}^h}(y_k,t)$ onto Chebychev polynomials leads to

$$\widehat{\mathbf{a^n}}(t) = \begin{bmatrix} \widehat{a_1^n}(t) \\ \vdots \\ \widehat{a_{M-4}^n}(t) \end{bmatrix} = \mathbf{\Sigma}^{-1}\begin{bmatrix} \widehat{V_{py}^{hn}}(y_3,t) \\ \vdots \\ \widehat{V_{py}^{hn}}(y_{M-2},t) \end{bmatrix}, \qquad \text{(A.10)}$$

where $\mathbf{\Sigma} = (\Sigma_i(y_k))_{i=5,...,M,\ k=3,...,M-2}$ is the combination of Chebychev basis evaluated at Gauss-Lobatto Collocation points (see McKernan (2006)).

Plugging (A.9) into (A.10) leads to

$$\widehat{\mathbf{a^n}}(t) = \mathbf{a^n}(t) + \frac{1}{N}\mathbf{\Sigma}^{-1}\begin{bmatrix} \varepsilon_3^{hn}(t) \\ \vdots \\ \varepsilon_{M-2}^{hn}(t) \end{bmatrix}, \qquad \text{(A.11)}$$

since $\mathbf{a^n}(t) = \mathbf{\Sigma}^{-1}\begin{bmatrix} V_{py}^{hn}(y_3,t) \\ \vdots \\ V_{py}^{hn}(y_{M-2},t) \end{bmatrix}$. Finally by letting $\mathbf{p^n}(t) = \begin{bmatrix} \mathbf{a^n}(t) \\ q_u^n(t) \\ q_l^n(t) \end{bmatrix}$ and $\mathbf{e^n}(t) = \begin{bmatrix} \mathbf{\Sigma}^{-1}\begin{bmatrix} \varepsilon_3^{hn}(t) \\ \vdots \\ \varepsilon_{M-2}^{hn}(t) \end{bmatrix} \\ \frac{1}{f_u(y_1)}\varepsilon_1^n(t) \\ \frac{1}{f_l(y_M)}\varepsilon_M^n(t) \end{bmatrix}$, it is easy to express the estimated coefficient $\widehat{\mathbf{p^n}}(t)$ in terms of the ideal one and the noise as given in (9).